

Far-Ultraviolet & X-ray Observations of VV 114: Feedback in a Local Analog to Lyman Break Galaxies

Accepted for Publication in ApJ

J. P. Grimes¹, T. Heckman¹, C. Hoopes¹, D. Strickland¹, A. Aloisi², G. Meurer¹, and A. Ptak¹

ABSTRACT

We have analyzed *FUSE*, *XMM-Newton*, and *Chandra* observations of VV 114, a local galaxy merger with strong similarities to typical high-redshift Lyman Break Galaxies (LBGs). Diffuse thermal X-ray emission encompassing VV 114 has been observed by *Chandra* and *XMM-Newton*. This region of hot ($kT \sim 0.59$ keV) gas has an enhanced α/Fe element ratio relative to solar abundances and follows the same relations as typical starbursts between its properties (luminosity, size, and temperature) and those of the starburst galaxy (star formation rate, dust temperature, galaxy mass). These results are consistent with the X-ray gas having been produced by shocks driven by a galactic superwind. The *FUSE* observations of VV 114 show strong, broad interstellar absorption lines with a pronounced blueshifted component (similar to what is seen in LBGs). This implies an outflow of material moving at $\sim 300 - 400$ km/s relative to VV 114. The properties of the strong O VI absorption line are consistent with radiative cooling at the interface between the hot outrushing gas seen in X-rays and the cooler material seen in the other outflowing ions in the *FUSE* data. We show that the wind in VV 114 has *not* created a “tunnel” that enables more than a small fraction (< few percent) of the ionizing photons from VV 114 to escape into the IGM. Taken together, these data provide a more complete physical basis for understanding the outflows that seem to be generic in LBGs. This will lead to improved insight into the role that such outflows play in the evolution of galaxies and the inter-galactic medium.

Subject headings: galaxies: starburst — galaxies: halos — UV: galaxies — galaxies: individual (VV114)

¹Center for Astrophysical Sciences, Johns

Hopkins University, 3400 N. Charles St, Bal-

1. Introduction

In recent years, progress in cosmology has been driven by the remarkable results of experiments such as *WMAP* (Bennett et al. 2003). These experiments have made precise measurements of the geometry, the age, and the spectrum of density fluctuations of our universe. Using Λ Cold Dark Matter (Λ CDM) numerical simulations, we can track the evolution of the large scale structure of the dark matter from the era of quantum fluctuations to our current epoch (e.g. Davis et al. 1985; Springel et al. 2005). However, significant problems in the simulations emerge when examining small scale structure and regions of high density where the complex range of baryonic physics becomes important (Klypin et al. 1999; Robertson et al. 2005; Sommer-Larsen et al. 1999). The next step forward in cosmology will therefore require a much better understanding of the physical processes involved in the interactions within the gas/star/black-hole ecosystem.

Feedback, powered by star formation, could play a crucial role in understanding galaxy formation and evolution. This is particularly true in past epochs, when the overall cosmic star formation rate was significantly higher (Bunker et al. 2004). In regions of intense star formation, short lived massive stars produce stellar winds and supernovae whose kinetic energy can collectively drive galactic scale outflows of metal enriched material into the galaxy

halo and potentially into the Intergalactic Medium (IGM, Aguirre et al. 2005). These "superwinds" can also enhance the fraction of ionizing radiation that escapes from the galaxy into the IGM (Dove et al. 2000). Therefore these complicated multi-phase winds are an important influence on the chemical and thermodynamical nature of the IGM. They are also likely to play a crucial role in the evolution of galaxies, particularly for low mass systems whose relatively shallow potential wells make them especially vulnerable to wind-driven loss of gas and metals (Tremonti et al. 2004).

Multiwavelength observations are required to understand the complex multi-phase nature of galactic winds. The coronal gas ($T \sim 10^5$ to 10^6 K) and hot X-ray gas ($T \sim 10^6$ to 10^7 K) in galactic winds are particularly important. These phases are intimately connected to the mechanical/thermal energy that drive the outflows and to the metals the outflows carry. Far-ultraviolet (FUV) observations of the coronal gas provide important insights into the cooling and kinematics of the galactic winds (Heckman et al. 2001a). X-ray observations probe the slowly cooling hot gas which is most likely to escape the galaxy (Strickland & Stevens 2000).

The most widely studied population of high redshift star forming galaxies are the Lyman Break Galaxies (LBGs, Steidel et al. 1999). These galaxies can be efficiently detected for $2 \lesssim z \lesssim 6$ using the Lyman-break technique which picks out spectral band dropouts caused by the 912 Å Lyman continuum discontinuity. They constitute a significant (and possibly dominant) fraction of the population of star forming galaxies during this important cos-

timore, MD 21218; jgrimes@pha.jhu.edu, heckman@pha.jhu.edu, choopes@pha.jhu.edu, dks@pha.jhu.edu, meurer@pha.jhu.edu

²Space Telescope Science Institute, 3700 San Martin Drive, Baltimore, MD, 21218; aloisi@stsci.edu

mic epoch (Peacock et al. 2000). Galactic winds appear to be a ubiquitous property of LBGs (Shapley et al. 2003). The LBGs trace the most overdense regions of the universe, which are believed to be the progenitors of present day galaxy clusters (Giavalisco 2002). They therefore play an important role in understanding the evolution of such clusters. In particular, winds from LBGs could be the process that heats and chemically enriches the Intercluster Medium (ICM, Helsdon & Ponman 2000; Tamura et al. 2004).

Unfortunately, our knowledge about the properties of the winds in LBGs is limited to what can be inferred from the interstellar UV absorption lines longward of Lyman α . Because of their great distance, X-ray detections are almost impossible using current X-ray observatories. Stacking techniques have been used to construct luminosity weighted average X-ray spectra (Nandra et al. 2002; Lehmer et al. 2005). A more fundamental problem is that the large redshifts of the LBGs mean that soft X-ray observations with *Chandra* or *XMM-Newton* are observing at rest-frame energies above a few keV. In local star-forming galaxies the emission in this band is dominated by the population of X-ray binaries, and the thermal emission from the galactic wind is negligible (Colbert et al. 2004). Likewise, observations of the coronal phase gas is very difficult in LBGs. The most accessible probe of such gas is the FUV O VI $\lambda\lambda 1032, 1038$ doublet which lies deep within the Lyman α forest in the spectra of LBGs.

It is clear that directly studying gas hotter than 10^5 K in high-redshift LBGs will continue to be very difficult or even impos-

sible for the foreseeable future. Therefore, an important step in understanding galactic winds in LBGs would be to identify the best local analogs to LBGs and to then investigate their winds using the full suite of observations that are possible at low redshift.

Recently Heckman et al. (2005) created a catalog of low redshift galaxies using *GALEX* (Martin et al. 2005) UV observations of galaxies with spectra taken by the Sloan Digital Sky Survey (SDSS, York et al. 2000). This catalog has now been significantly expanded based on additional *GALEX* data by Hoopes et al. (2006). They used this matched catalog to select a sample of extraordinarily rare local ($z < 0.3$) galaxies having the same UV luminosities, sizes, and surface brightnesses as typical LBGs. They then showed that these galaxies have the same star formation rates (SFRs), galaxy masses, velocity dispersions, and chemical compositions as typical LBGs. Based on the sample observed to date with *GALEX*, VV 114 at $z \sim 0.02$ is the closest known LBG analog, thus making it ideal for X-ray and FUV studies.

HST NICMOS and STIS observations by Goldader et al. (2002) of VV 114 (ARP 236) have shown two distinct interacting/merging components to the galaxy. The two components are separated by 6 kpc in projection ($\sim 15''$). The eastern component, while prominent in the NIR NICMOS images, is almost invisible in the STIS UV images due to heavy dust obscuration. The western component is very bright in the UV, with a far-UV luminosity of $2.2 \times 10^{10} L_\odot$, half light radius of 2.3 kpc, and effective mean surface brightness

of $6 \times 10^8 L_\odot/\text{kpc}^2$, all comparable in value to those of LBGs (Heckman et al. 2005). CO (1-2) observations by Yun et al. (1994) show that the molecular gas is centered between the two components of VV 114. Their measured velocities of the molecular gas coincident with the western component show a rotating disk with a velocity range between 5900 km/s and 6200 km/s. Yun et al. (1994) also show, from 1.4 GHz radio continuum observations, that star formation is spread throughout the VV 114 system. The NIR, MIR and CO (3-2) emission of VV 114 is dominated by a source at the center of the eastern component. Combinations of compact star formation (Iono et al. 2004) and an obscured AGN (Le Floc'h et al. 2002) have been used to explain the emission. The observed IRAS $L_{\text{FIR}} \sim 2.8 \times 10^{11} L_\odot$ (Soifer, Boehmer, Neugebauer, & Sanders 1989) is then a measure of the entire system's SFR and implies a total SFR of $\sim 48 M_\odot$ per year (Kennicutt 1998). Goldader et al. (2002) suggest that the star formation is split roughly equally between the two components. These properties are summarized in Table 1.

2. The Data

2.1. *FUSE* Observations & Analysis

The *FUSE* spacecraft is composed of four separate mirrors and two detectors (Moos et al. 2000). Two mirrors are coated with LiF and two with SiC. The LiF mirrors have better sensitivity in the $1000 \text{ \AA} \lesssim \lambda \lesssim 1180 \text{ \AA}$ wavelength region while the SiC are optimized for observations in the range between 900 \AA to 1000 \AA . Observation pointing is controlled by a Fine Er-

ror Sensor (FES) camera located along the LiF1 channel which results in a pointing rms of $\sim 0.5''$.

FUSE observed VV 114 ($\alpha_{2000} = 01^h 07^m 46^s.60$, $\delta_{2000} = -17^\circ 30^m 24^s.0$) using the LWRS aperture ($30'' \times 30''$) on July 26, 2003. The observations were centered on the FUV emitting western component of VV 114. The *FUSE* aperture is shown overlayed on the *HST STIS* FUV (F25SRF2) observation of VV 114 in Figure 1.

The *FUSE* observation of VV 114 was split into five exposures. For every exposure and detector segment a raw time-tagged event list was produced. We processed each event list using the latest *FUSE* calibration software, CALFUSE v3.1.2 (Dixon & Sahnow 2003). This software applies flux and wavelength calibrations while correcting for a variety of effects including instrument motion, geometric distortions, spacecraft doppler shifts, event bursts, and the South Atlantic Anomaly (SAA).

The Hydrogen Lyman series absorption lines dominate the spectrum below $\sim 1000 \text{ \AA}$ so we have focused on the longer *FUSE* wavelengths. As the LiF channels have a greater sensitivity and thus better S/N we have ignored the SiC channels in our data analysis. A comparison of the LiF1 guiding channel to the LiF2 channel confirms that channel drift is negligible for our data. In order to co-add the spectra we cross correlated the spectra to correct for small wavelength shifts. Also, as the count rate is significantly lower in the first exposure, we have excluded it from the final combined spectra for each channel. This produces four combined spectra, LiF1A and LiF2B covering $\sim 985 \text{ \AA} - 1075 \text{ \AA}$ and

LiF1B and LiF2A in the range between $\sim 1090 \text{ \AA} - 1185 \text{ \AA}$. The best spectrum in each of the two wavelength regions is shown in Figure 2. We have also labeled the most prominent FUV ISM absorption lines, stellar photospheric lines, Milky Way absorption lines, and airglow features. The spectra around several of the most prominent ISM absorption lines are shown in Figure 3.

An examination of the spectrum of VV 114 shows that it is dominated by broad ISM absorption lines. The strongest lines (e.g. Ly β , C III $\lambda 977$, C II $\lambda 1036$) are saturated in their cores. Most of the strong, higher S/N lines show common structures in their profiles. This can be seen in Figure 4 where we have vertically aligned the N II $\lambda 1084$, C II $\lambda 1036$, and N I $\lambda 1134$ absorption lines. Some of the small scale absorption features are found at ~ 6300 , 6100, and 5900 km/s. The 6300 km/s component is interesting as it could be infalling material or non-circular motion from the ongoing merger of the two galaxy components. More important however is the general shape of the absorption line profiles. All three lines in Figure 4 are asymmetric, with a pronounced wing of blueshifted absorption extending down to ~ 5000 km/s.

To fit the lines we used the iraf tool *specfit* (Kriss 1994). Initially, each line was fit separately using a freely variable powerlaw for the continuum and a symmetric gaussian absorption line. As we have double coverage of most wavelength regions, we independently measure most of the absorption lines and continuum twice. For many of the lines, the line width (FWHM) is not well constrained so we have fixed it to 700 km/s which is a value consistent

with our fits to the strong lines. Some additional complications are also important to note. The C II $\lambda 1036$ and O I $\lambda 1039$ lines are mildly blended so we have fixed the central velocity of the O I $\lambda 1039$ line relative to that of the C II. We then tied the two FWHMs together and fit the two lines. We used the same approach with the two strongly blended lines, O I $\lambda 989$ and N III $\lambda 990$. Although we were able to fit these two lines, they are badly blended and so there is a significant uncertainty in our derived parameters. Table 2 shows the results of our fits to the data. Errors are one σ and are calculated from a rescaled inversion of the curvature matrix. There are a few weak lines in the spectra that we have not fit due to their low S/N.

The single component fits above do not account for the blueshifted component clearly seen in the higher S/N absorption lines. Therefore, for the strongest lines (e.g. C II, N II, N I, O I) we have refit the data with a second blueshifted gaussian absorption line. We have excluded the strongly blended lines O I $\lambda 989$ and N III $\lambda 990$ and the heavily saturated Lyman β and C III $\lambda 977$ lines from these new fits. O VI was also excluded as it clearly has a different line profile than the other strong lines (see below). The 2-component fits are shown in Figure 4 and Table 3 and significantly improve the fit quality of each line. The results for the different lines are all consistent with a strong absorption line at ~ 6050 km/s with a second blueshifted line at ~ 5650 km/s. The blueshifted component generally has an equivalent width of typically about 0.4 that of the principal component and a marginally smaller FWHM. The success

of the two absorption component fits suggests an inadequacy in the single line fits. This provides a caution in using the single line fits to determine central velocities of the absorption lines. The blueshifted component is probably a general feature, but is not conspicuous in the weaker lines due to their lower S/N.

Several prominent stellar photospheric absorption lines are observed in the data. These lines allow us to independently constrain the velocity of the UV emitting portion of VV 114. We have fit these absorption lines in the same manner as described above. The line centroids were tied together in order to strongly constrain the relative velocity. Our fit results can be found in Table 4. The fitted FWHMs of the photospheric lines are significantly narrower at 390 km/s than the ISM FWHMs (~ 700 km/s). Combining the measurements we find a system velocity of 5971 ± 14 km/s.

2.2. *Chandra* Observations

VV 114 was observed by *Chandra* on October 20, 2005. The data was obtained using very faint mode with the galaxy centered on the ACIS S3 aim point. Standard data processing was applied using CALDB 3.1.0 and ASCDSVER 7.6.3 (Chandra Interactive Analysis of Observations CIAO). Less than 1 ks of observation time was lost due to anomalous background levels leaving 58.8 ks of total integration time.

For image and spectral analysis we followed the same procedures as previously described in Grimes et al. (2005). Using an image of the counts in the 0.3 - 1.0 keV range we calculated a 90% counts enclosed radius for VV 114 of 4.4 kpc. The 0.3 -

1.0 keV band was chosen as it is sensitive to the diffuse thermal emission and minimizes point source contamination. We also created adaptively smoothed images using the CIAO task CSMOOTH. For all of our spectral analysis a local background was used. The background was centered on the galaxy but excluded all diffuse and point source emission. Spectra were extracted using the CIAO script SPECEXTRACT and grouped using a minimum of 20 counts per bin.

The high spatial resolution *Chandra* counts (0.3-8.0 keV) image in Figure 5 has several interesting features. Both the eastern and western components are clearly observed. The western component dominates the X-ray emission and has a similar morphology to that seen in the STIS data. The peak of the X-ray emission coincides with the brightest star cluster seen in the UV. Diffuse X-ray emission is seen to the south of the galaxy and extends far beyond the limits of the FUV and NIR emission.

Figure 6 shows an adaptively smoothed *Chandra* false color image of the galaxy. The emission from VV 114E is harder than that from the western component. This is consistent with the high column densities suggested by the FUV observations (Figure 1). Soft X-rays from VV 114E are absorbed so that, as in the FUV, the soft X-ray emission is primarily tracing VV 114W. Figure 7 has a soft band image of the entire galaxy with a blown up picture of the inner regions in the hard band. A compact source is also detected near the center of VV 114E. It is coincident with the unresolved source seen in the NICMOS and lower resolution Spitzer IRAC images.

The spectra were well fit by a model

that included an absorption column, a thermal plasma model, and an absorbed powerlaw. XSPEC's vmekal model was used which allows for variable metallicities. The derived model fit parameters are listed in Table 5 while the data and fit are plotted in Figure 8. Following Grimes et al. (2005) we have only calculated the α/Fe ratio due to degeneracies in the model fit in determining the absolute elemental abundances. The α/Fe ratio of $2.7^{+0.6}_{-0.7}$ (90% confidence) assumes the default XSPEC solar abundances of Anders & Grevesse (1989). More recent abundance measurements from Asplund et al. (2005) obtain comparable results with an α/Fe ratio of $2.5^{+0.8}_{-0.3}$. The 0.3 - 2.0 keV luminosity of the thermal emission VV 114E is 2.2×10^{41} erg s $^{-1}$.

2.3. *XMM-Newton* Observations

The *XMM-Newton* data was retrieved from the US public archive at HEASARC, and analyzed using version 5.3 of the Standard Analysis System (SAS). The latest calibration files available at the time were used. Images and spectra were extracted from the MOS1 and MOS2 events files produced by the XMM-Newton data pipeline, with total exposures of 11367 and 11348 seconds respectively. No data from the PN detector was available. The spectra of VV 114 included all events within a radius of 30" of the peak in the soft X-ray emission seen in the X-ray images, which closely coincides with the NED position for VV 114. A background spectrum was taken in an annulus of inner and outer radii 40" and 80" respectively. The spectra was subsequently analyzed using XSPEC 11.2.

We simultaneously fit the MOS1 and MOS2 spectra using the same model as

for the *Chandra* data. Table 5 lists the derived model parameters while Figure 8 shows the unfolded spectra and model components. The results of the *XMM-Newton* fit are consistent with those from the longer exposure, higher quality *Chandra* data. The derived vmekal plasma temperature is $0.59^{+0.06}_{-0.09}$ keV with an α/Fe ratio of $2.2^{+2.0}_{-0.7}$ (abundances from Anders & Grevesse (1989)). The Asplund et al. (2005) abundances obtain similar results with an α/Fe ratio of $1.5^{+1.9}_{-0.6}$ (90% confidence). We've also derived the absorption corrected luminosity of the thermal plasma as 2.0×10^{41} erg s $^{-1}$ in the 0.3-2.0 keV energy range.

3. Discussion

3.1. AGN and Starburst Activity in VV 114E

While the western component of VV 114 dominates the UV and X-ray emission, VV 114E is the more powerful near-IR emitter (right panel in Figure 6). NIR spectral observations by Doyon et al. (1995) show evidence of a gas photoionized by $\sim 4 \times 10^5$ OB stars in VV 114E. The extended emission observed in the radio (Condon et al. 1991) and NIR (Doyon et al. 1995) bolster the argument that a compact starburst dominates VV 114E. Le Floc'h et al. (2002) however observed a continuum bump at 5-6 μm which is typical of AGN spectra. They suggest that a heavily absorbed AGN could contribute up to 40% of the mid-IR flux in VV 114E.

We extracted *Chandra* spectra of a small circular region surrounding VV 114E. The extracted spectra can be seen in Figure 9. This region encloses roughly 600

counts, about 10% of the total counts observed in VV 114. The spectra is heavily absorbed requiring $N_H \approx 2 \times 10^{22} \text{ cm}^{-2}$. A fairly flat powerlaw is also fit with a photon index of ~ 1.3 , consistent with the existence of a buried AGN.

We initially fit the lower energy spectra of VV 114E with a simple absorbed thermal plasma model with variable abundances. This provides a poor fit and requires abundances of over 13 times solar values. The super-solar abundances are driven by the enhanced Si ($\sim 1.4 \text{ keV}$) and Mg ($\sim 1.8 \text{ keV}$) line emission. This is typical in photo-ionization regions and is seen in stellar winds from high-mass X-ray binaries (HMXBs, Sako et al. 2002), OB stars (Oskinova et al. 2006), and some obscured AGN (Levenson et al. 2006). The addition of two gaussians to the model fit results in reasonable sub-solar abundances and a significantly better fit with a reduced $\chi^2 \sim 0.8$ (Figure 9).

The thermal plasma dominates the emission in the 0.3-2.0 keV range with an unabsorbed luminosity of $2 \times 10^{41} \text{ ergs s}^{-1}$. The eastern component's thermal plasma luminosity of $2 \times 10^{41} \text{ ergs s}^{-1}$ is comparable to the luminosity we inferred for the **entire** galaxy in section 2.2. As the observed photons are primarily from the unabsorbed western component a successful model can ignore the heavily absorbed eastern component. However, this causes us to underestimate the soft X-ray luminosity of VV 114 by a factor of ~ 2 . This complication does not occur in the harder X-ray range where we derive the 2-10 keV luminosities for the eastern and western components as $1.1 \times 10^{41} \text{ erg s}^{-1}$ and $1.3 \times 10^{41} \text{ erg s}^{-1}$ respectively. Previous works (Bauer et al.

2002; Franceschini et al. 2003) have shown that the hard X-ray emission can be used as a SFR tracer. Assuming the hard X-ray emission is tracing HMXBs and not contaminated by an AGN we can derive the SFR for the two galaxy components. This implies that they have a roughly equal star formation rate with $\sim 28 M_\odot/\text{year}$ for VV 114E and $\sim 33 M_\odot/\text{year}$ for VV 114W (Franceschini et al. 2003). The total star formation rate of $\sim 61 M_\odot/\text{year}$ (30% scatter) is consistent with the $\sim 48 M_\odot/\text{year}$ inferred from the FIR luminosity suggesting that star formation is the dominant energy source.

An AGN contribution however is still not ruled out. Although Fe K α emission is not observed in the binned (minimum 20 counts) spectra of VV 114E, we have extracted an image in the 6.25-6.55 keV range. A single feature, centered on the unresolved source in the *Chandra* and NICMOS images, is visible. The five detected counts are well above the expected contribution from the background plus the fitted powerlaw of less than 0.01 counts. We extracted unbinned spectra from circular region with a diameter of $2.3''$ (1 kpc) and centered on the unresolved source in VV 114E. We fit the spectra with a gaussian centroided at 6.4 keV and found a best fit equivalent width of 0.3 keV. As the gaussian is poorly constrained, we have instead found a 90 % confidence level upper limit on the equivalent width of 1.3 keV. The luminosity in the Fe K α line is $1.3 \times 10^{40} \text{ erg s}^{-1}$.

Levenson et al. (2006) have studied a sample of heavily absorbed AGN and found that the IR and Fe K α emission line luminosities are correlated with $\log(L_{\text{IR}}/L_{\text{Fe K}\alpha}) \approx 3.5$.

For VV 114 this would suggest a 90 % confidence upper limit to the AGN contribution of $L_{\text{IR}} < 1 \times 10^{10} L_{\odot}$. This is significantly less than the $L_{\text{IR}} \sim 5 \times 10^{11} L_{\odot}$ observed by IRAS. This supports the idea that a compact nuclear starburst dominates the central region of VV 114E. The weak detection of Fe K α is also consistent with the nuclear starburst argument. We note that Fe K α lines are detected in HMXBs (Sako et al. 2002). Assuming that the 2.0 - 10 keV luminosity is not contaminated by an AGN, almost one quarter of the SF in the entire galaxy is concentrated within a region 1 kpc in diameter at the center of VV 114E.

We conclude that while a highly obscured AGN *may* be present in the nucleus of VV 114E, it would not contribute significantly to the bolometric luminosity of the VV 114 system. The energetics of VV 114 are instead dominated by the intense episode of star formation it is undergoing.

3.2. *FUSE* Observations of the Wind

The success of the two component fits to the absorption line profiles suggest a simple dynamical picture. The stronger absorption feature at ~ 6050 km/s traces the ISM of VV 114W. This velocity is consistent with that of the molecular gas of the western component. The stellar absorption lines, which we would also expect to be associated with the western component, appear to be at a slightly lower central speed of ~ 5970 km/s. This difference in velocities could be explained by a systematic error in the two component absorption model caused by degeneracy in some of the fit parameters. A difference in the relative spatial distribution between the hot

stars and ISM and the way they sample the galaxy rotation curve could also explain this small velocity shift. The blueshifted ISM absorption feature has a mean velocity of ~ 5650 km/s, implying an outflow of gas moving at a mean velocity of ~ 300 -400 km/s away from the galaxy. Weaker absorption can be seen at velocities as low as ~ 5000 km/s (e.g. N I and O I), suggesting that the wind is accelerating clouds up to outflow velocities as high as ~ 1000 km/s.

It is important to compare our results to previous absorption line studies of LBGs. In the composite LBG spectrum created by Shapley et al. (2003) they measure broad (FWHM ~ 550 km/s) and blueshifted ($v \sim 150$ km/s) ISM absorption lines. In the observations of CB58 by Pettini et al. (2002) they find a mean outflow speed of $v = 255$ km/s and slightly broader lines. Both these results are consistent with what we observe in VV 114.

It is also interesting that the kinematics of the coronal gas as traced by the O VI absorption line is different from what is seen in the cooler gas. In the single absorption component fits the centroid of the O VI absorption line is blueshifted by about 100 km/s compared to the other strong lines, and the line profile is much more symmetric. Absorption in O VI can be seen at velocities as low as ~ 5000 km/s, consistent with outflow velocities as high as ~ 1000 km/s. Unfortunately, the blue wing of the O VI line merges with the red wing of the adjacent Lyman β line, making it impossible to tell if even faster moving coronal gas might be present.

The different kinematics of the O VI line implies a different physical origin. The O VI line is a particularly interesting one

due to its importance in radiative cooling and the relatively narrow temperature range over which it is a significant ion. Heckman et al. (2001a) also observed O VI absorption in the dwarf starburst NGC 1705. In NGC 1705 the O VI line was also more strongly blueshifted than the other ions. They attributed the production of O VI to the intermediate temperature regions created by the hydrodynamical interaction between hot outrushing gas and the cool fragments of the ruptured superbubble seen in H α images. Such a situation is predicted to be created as an overpressured superbubble accelerates and then fragments as it expands out of the galaxy.

Heckman et al. (2002) derive a simple and general relationship between the O VI column density and absorption line width which will hold whenever there is a radiatively cooling gas flow passing through the coronal temperature regime. They showed that this simple model accounted for the properties of O VI absorption line systems as diverse as clouds in the disk and halo of the Milky Way, high velocity clouds, the Magellanic Clouds, starburst outflows, and the clouds in the IGM. Using the measured equivalent width in Table 2 we have measured an O VI column density of $\log(N_{\text{OVI}}) = 15.3$. Figure 10 shows the predictions and data from Heckman et al. (2002) and includes VV 114. VV 114 has the both the highest O VI column density and broadest line width in the plot, and is fully consistent with the model predictions. It would then trace radiatively cooling gas in a high speed outflow.

For the outflow components, it is interesting to estimate the mass and energy

outflow rates. We follow Heckman et al. (2000) and assume a mass-conserving outflow with a constant velocity. This allows us to estimate the mass and energy outflow rate in the wind from the total gas column density, outflow velocity and starburst radius (equations 5 and 6 in Heckman et al. (2000)). To estimate the gas column density in the outflow we use ionic column densities for the blueshifted wind component derived from the strongest unsaturated lines. We then convert these into hydrogen column densities assuming solar abundances from Asplund et al. (2005). The Oxygen abundances of $12 + \log[\text{O}/\text{H}] = 8.6$ and 8.7 (Kim et al. 1995; Charlot & Longhetti 2001) for the two most prominent knots in VV 114W suggests that this is reasonable. The hydrogen column density in the neutral gas can be measured from both N I and C II. Both predict a column density of about $\sim 6 \times 10^{18} \text{ cm}^{-2}$. The N II column density leads to a corresponding ionized hydrogen column density of $1.4 \times 10^{19} \text{ cm}^{-2}$. This is a lower limit since we make no correction for more highly ionized nitrogen. Finally, O VI predicts a lower limit to the hydrogen column of the coronal phase of the outflow of $2.3 \times 10^{19} \text{ cm}^{-2}$, based on the maximum possible O VI ionic fraction of $\sim 20\%$ for collisional ionization equilibrium (Sutherland & Dopita 1993). The lower bound to the total hydrogen column density in the outflow is then $\sim 4 \times 10^{19} \text{ cm}^{-2}$. Taken a starburst radius of 2.3 kpc ($R_{50,\text{UV}}$), and an outflow velocity of 400 km/s we find an mass outflow rate of $\sim 5 \text{ M}_\odot$ per year and a kinetic energy outflow rate of $\sim 2.5 \times 10^{41} \text{ erg/sec}$ (assuming a wind opening angle of 4π steradians). The derived values are in Table 6. To put these values into context,

in section 3.1 we estimated the star formation rate of VV 114W as roughly $24\text{--}33\text{ M}_\odot$. The implied star formation rate is of order the outflow rate. The total rate at which supernovae and stellar winds provide mechanical energy in VV 114W is $\sim 6 \times 10^{42}$ erg/sec, and the estimated energy outflow rate is therefore only $\sim 5\%$ of the total. These results are similar to what is seen in typical far-IR luminous starburst galaxies based on the interstellar NaI D absorption-line (Heckman et al. 2000; Rupke et al. 2005; Martin 2005).

3.3. Physical Properties of the Hot Phase of the Wind

We can use the parameters for the fit to the total Chandra and XMM X-ray spectra of the diffuse gas in VV 114 to derive estimates for the basic physical properties of the hot phase of the wind. The normalization for the VMEKAL component implies an emission integral (the volume integral of density squared) of $2.4 \times 10^{64} \text{ cm}^{-3}$. For the geometrical volume of the emitting region we take a sphere whose radius encompasses 90% of the soft X-ray emission ($\sim 4.5 \text{ kpc}$). This then implies a mean gas density of $n \sim 5 \times 10^{-2} f^{-1/2} \text{ cm}^{-3}$ and a gas mass of $M \sim 4 \times 10^8 f^{1/2} \text{ M}_\odot$ (where f is the volume filling factor of the X-ray emitting material). For $kT = 0.59 \text{ keV}$ the mean thermal pressure is $P = 1.3 \times 10^{-10} f^{-1/2} \text{ dynes cm}^{-2}$ and the total thermal energy content of the hot gas is $E = 1.4 \times 10^{57} f^{1/2} \text{ ergs}$.

Taking the characteristic timescale to be the above radius (4.5 kpc) divided by the sound speed in the hot gas ($\sim 500 \text{ km/sec}$) yields an age of 9 Myr. The implied outflow rates in the hot gas are then

$\dot{M} \sim 50 f^{1/2} \text{ M}_\odot/\text{year}$ and $\dot{E} \sim 5 \times 10^{42} f^{1/2} \text{ erg/sec}$. For volume filling factors similar to those estimated for other starburst winds ($f \sim 0.1$ to 1), the implied mass outflow rate in VV 114 is comparable to the total star formation rate ($\sim 30 \text{ M}_\odot/\text{year}$) and the rate of energy transport is comparable to the total rate at which mechanical energy would be supplied by supernovae and stellar winds in the starburst ($\sim 10^{43} f^{1/2} \text{ erg/sec}$). These outflow rates significantly exceed the rates for the cooler gas derived from the *FUSE* data above, but are typical of winds in powerful local starburst galaxies (e.g. Heckman 2003).

3.4. X-ray Properties Compared to SF Galaxies

In Grimes et al. (2005) we studied the X-ray properties of 22 star forming galaxies spanning over 4 orders of magnitude in X-ray luminosity including ULIRGs like Arp 220, normal starbursts like M 82, and dwarf starbursts like NGC 1705. Our principal conclusion was that the properties of the hot gas in all of these star forming galaxies were remarkably similar. In general, simple scaling relations were able to explain many of the differences between the galaxies in the sample. These relationships are consistent with the basic superwind scenario in which the mechanical energy deposited by stellar winds and supernovae results in an over-pressurized cavity of hot gas within the starburst. The cavity will expand, driving the hot gas outwards, possibly out of the galaxy and into the surrounding IGM.

In our study we saw that the luminosity of the diffuse soft X-ray emission was roughly linearly proportional to the SFR

(e.g. L_{FIR}). VV 114 is no exception as can be seen in Figure 11. In this figure we have divided both the FIR and X-ray luminosities by the K-Band luminosity. By dividing by the K-band luminosity, a proxy for stellar mass, we show that it is not merely a matter of more massive galaxies having higher SFRs and X-ray luminosities. The linear scaling between X-ray luminosity and L_{FIR} suggests a constant efficiency in converting mechanical energy from the galactic winds into emission from hot gas. The size scale of the region of X-ray emission will also depend upon the rate at which the starburst supplies mass and energy to the wind, and this relation is shown in Figure 12 where we have plotted the 90% X-ray flux (0.3-1.0 keV) enclosed radius vs the FIR luminosity. Again, VV 114 follows the same trends seen in the other starbursts.

In Grimes et al. (2005) we also showed there was a trend for the starbursts with the highest SFR per unit area (as traced by the FIR color-temperature of the warm dust) to have the hottest X-ray gas. Again VV 114 is consistent with this trend, as shown in Figure 13. Lastly, in agreement with the starbursts in Grimes et al. (2005), VV 114 appears to have an α/Fe element ratio that is enhanced (by a factor of ~ 2) relative to solar abundances. An enhanced α/Fe element ratio would be expected in a starburst galaxy as the hot gas could be significantly enriched by the material injected by the core-collapse supernovae driving the winds (e.g. Marcolini et al. (2005)).

It is interesting to compare VV 114 to the ULIRGs. Although it follows the same scaling relations as the ULIRGs it does not appear to live in the same parameter space.

Obviously, it has a lower FIR luminosity and thus SFR. It also has a slightly smaller but similar K-Band luminosity than the average ULIRGs (and hence a correspondingly similar stellar mass). Lastly VV 114 has slightly lower gas and dust temperatures than the ULIRGs. This suggests that VV 114 is a similar mass galaxy with a lower SFR per unit area than the ULIRGs and is intermediate between the normal starbursts and ULIRGs.

3.5. Escape of Ionizing Radiation

One of the major puzzles in cosmology is the nature of the objects responsible for the reionization of the universe, which may have started as early as $z \sim 30$ and was complete by $z \sim 6$ (Loeb & Barkana 2001). The known population of AGN do not appear to be sufficient by a wide margin, and the leading candidates are star forming galaxies (Stiavelli et al. 2004; Panagia et al. 2005). Steidel et al. (2001) reported the detection of a significant flux of ionizing radiation escaping from LBGs based on the detection of flux in the rest-frame Lyman continuum. However, other studies of high- z star forming galaxies have reached different conclusions (e.g. Malkan et al. 2003).

There have been several attempts to measure the fraction of the ionizing radiation escaping from local starbursts (f_{esc}). The hope is that investigations of local star forming galaxies will allow us to understand the physical processes that determine f_{esc} so that we can apply these lessons to high redshift galaxies for which our information is less complete.

Leitherer et al. (1995) reported the first direct measurements of f_{esc} using the Hop-

kins Ultraviolet Telescope to observe below the rest-frame Lyman edge in a sample of four local starbursts, and these data were later reanalyzed by Hurwitz et al. (1997). The resulting upper limits on f_{esc} were typically 10%. Deharveng et al. (2001) have obtained similar data with FUSE for the starburst galaxy Mrk 54 at $z = 0.0448$. No flux was detected below the Lyman edge in the rest frame. By comparison with the number of ionizing photons derived from the H α line, they set an upper limit to f_{esc} of 6%.

Heckman et al. (2001b) used FUSE in a different way to constrain f_{esc} in a sample five of the UV-brightest local starburst galaxies. They showed that the strong C II $\lambda 1036$ interstellar absorption-line is black in its core. Since the photoelectric opacity of the neutral ISM below the Lyman-edge will be significantly larger than in the C II line, they were able to use these data to set a typical upper limit on f_{esc} of 6% in these galaxies. Inclusion of absorption of Lyman continuum photons by dust grains will further decrease f_{esc} (by up to an order of magnitude in some cases). They also assessed the idea that strong galactic winds can clear channels through the neutral ISM of the galaxy and thereby increase f_{esc} (e.g. Fujita et al. 2003).

Given the presence of a strong wind in VV 114 and the overall similarity between VV 114 and typical LBGs, it is interesting to determine f_{esc} in this object. As can be seen in Figures 2 and 3, the C II $\lambda 1036$ line in VV 114 is quite black at line center. This is particularly striking as the large FUSE aperture samples all of the sightlines towards VV 114W. Following the precepts

of Heckman et al. (2001b) we find that f_{esc} is smaller than a few percent in VV 114W. The escape fraction decreases even further if we consider that all of the FUV radiation from VV 114E is also being absorbed.

In this aspect then, VV 114 is apparently quite different from the LBGs studied by Steidel et al. (2001). It also differs from Haro 11, which is the only local case known in which ionizing radiation is escaping from a galaxy (Bergvall et al. 2006). Since Haro 11 and VV 114 are similar in many ways, it will be important to understand why they are different in this crucial respect.

4. Conclusions

Understanding the role played by the feedback from star formation in the evolution of galaxies and the IGM is a crucial problem in cosmology (Fujita et al. 2004; Scannapieco et al. 2005). In the local universe, detailed observations of starburst galaxies have shown that this feedback is manifested most dramatically in the form of galactic winds that are driven by the collective effect of the kinetic energy supplied by winds from massive stars and supernova explosions. The outflows are complex multi-phase phenomena whose physical, chemical, and dynamical properties can only be understood through complementary observations at many wavebands (Veilleux et al. 2005). Observations of the coronal (10^5 to 10^6 K) and hot (10^6 to 10^7 K) gas are particularly important, as they provide essential information about the importance of radiative cooling of the outflow and about the dynamics and energy content of the wind. The coronal gas is best traced through the O VI doublet in

the far-UV and the hot g! as is best traced via its soft X-ray emission.

The strong overall cosmic evolution in the global star formation rate (Bunker et al. 2004) means that the bulk of the feedback from galactic winds occurred at early times ($z > 1$). Indeed, the direct signature of galactic winds – the presence of broad, blueshifted interstellar absorption lines in the rest-frame UV – is generically present in the Lyman Break Galaxies (LBGs, Shapley et al. 2003). These are the best-studied population of high-redshift star forming galaxies (Steidel et al. 1999). However, such data provide only a narrow range of information about galactic winds. Unfortunately, direct observations of the hotter gas in the rest-frame soft X-ray and FUV regions for high redshift galaxies are extremely difficult or even impossible, which hinders progress in understanding this complex phenomenon. Finding and studying nearby analogs to LBGs is therefore very important.

In this paper we have described FUV and soft X-ray observations of VV 114, the nearest known galaxy whose basic properties are a good match to those of typical LBGs (Heckman et al. 2005; Hoopes et al. 2006). Our *FUSE* observations in the FUV show strong and very broad interstellar absorption lines. The lines with the highest S/N show two kinematic components. One is centered near the galaxy systemic velocity and apparently corresponds to the galaxy ISM. The second component is strongly blueshifted, with a centroid 300 to 400 km/s below systemic velocity and weaker absorption extending to blueshifts as high as ~ 1000 km/s. This is consistent with what is seen at slightly longer rest

wavelengths in high redshift LBGs and further establishes the similarity of VV 114 to the LBGs. The O VI absorption line covers a similar range in velocity to the other ions, but has a much more symmetric profile. This suggests a different origin for the coronal-phase absorbing gas. The high column density and broad width of the O VI line are consistent with production of O VI in gas that is cooling radiatively from high temperature through the coronal regime. One possible origin for this gas is at the interface between the hot outflowing gas seen in X-rays and the cool clouds in the galaxy halo. These cooler clouds may be traced by the absorption lines from the cooler gas seen in the *FUSE* observations.

Observations with *XMM-Newton* and *Chandra* of the hot diffuse gas in VV 114 are consistent with those seen in a local sample of star forming galaxies with galactic outflows. As expected based on its far-IR luminosity and implied SFR, VV 114 has X-ray properties intermediate between those of ULIRGs and those of more typical present-day starbursts. This suggests that diffuse thermal X-ray emission should be a common feature of LBGs created in the shocks between the outflowing wind material and surrounding medium (Marcolini et al. 2005). Hard X-ray, far-IR, and radio continuum observations suggest that half of the star formation in VV 114 is not easily observable in the UV and soft X-ray as it is taking place in the heavily obscured eastern component of VV 114.

The strong wind in VV 114 might in principle be able to carve a channel in the ISM through which ionizing photons could escape from the starburst to the IGM. However, we show that the fact that the

core of the C II $\lambda 1036$ absorption line is black implies that the fraction of ionizing photons that escape from VV 114 is no more than a few percent. This low escape fraction in VV 114 is quite different from that seen in the LBGs studied by Steidel et al. (2001).

As the sample of nearby LGB-analogs discovered by GALEX grows, we will be able to eventually conduct multi-waveband investigations of the galactic winds in a sample large enough for us to be able to make robust statements about the physical, chemical, and dynamical properties of these objects. This should have important implications for the evolution of galaxies and the IGM.

REFERENCES

Aguirre, A., Schaye, J., Hernquist, L., Kay, S., Springel, V., & Theuns, T. 2005, ApJ, 620, L13

Anders, E., & Grevesse, N. 1989, Geochim. Cosmochim. Acta, 53, 197

Asplund, M., Grevesse, N., & Sauval, A. J. 2005, ASP Conf. Ser. 336: Cosmic Abundances as Records of Stellar Evolution and Nucleosynthesis, 336, 25

Bauer, F. E., Alexander, D. M., Brandt, W. N., Hornschemeier, A. E., Vignali, C., Garmire, G. P., & Schneider, D. P. 2002, AJ, 124, 2351

Bennett, C. L., et al. 2003, ApJS, 148, 1

Bergvall, N., Zackrisson, E., Andersson, B.-G., Arnberg, D., Masegoas, J., & Ostlin, G. 2006, A&A, 448, 513

Bunker, A. J., Stanway, E. R., Ellis, R. S., & McMahon, R. G. 2004, MNRAS, 355, 374

Carpenter, J. M. 2001, AJ, 121, 2851

Chandra Interactive Analysis of Observations (CIAO), <http://cxc.harvard.edu/ciao/>

Charlot, S., & Longhetti, M. 2001, MNRAS, 323, 887

Colbert, E. J. M., Heckman, T. M., Ptak, A. F., Strickland, D. K., & Weaver, K. A. 2004, ApJ, 602, 231

Condon, J. J., Huang, Z.-P., Yin, Q. F., & Thuan, T. X. 1991, ApJ, 378, 65

Davis, M., Efstathiou, G., Frenk, C. S., & White, S. D. M. 1985, ApJ, 292, 371

Deharveng, J.-M., Buat, V., Le Brun, V., Milliard, B., Kunth, D., Shull, J. M., & Gry, C. 2001, A&A, 375, 805

Dixon, W. V., & Sahnow, D. J. 2003, ASP Conf. Ser. 295: Astronomical Data Analysis Software and Systems XII, 295, 241

Dove, J. B., Shull, J. M., & Ferrara, A. 2000, ApJ, 531, 846

Doyon, R., Nadeau, D., Joseph, R. D., Goldader, J. D., Sanders, D. B., & Rowlands, N. 1995, ApJ, 450, 111

Le Floc'h, E., Charmandaris, V., Laurent, O., Mirabel, I. F., Gallais, P., Sauvage, M., Vigroux, L., & Cesarsky, C. 2002, A&A, 391, 417

Franceschini, A., et al. 2003, MNRAS, 343, 1181

Fujita, A., Martin, C. L., Mac Low, M.-M., & Abel, T. 2003, *ApJ*, 599, 50

Fujita, A., Mac Low, M.-M., Ferrara, A., & Meiksin, A. 2004, *ApJ*, 613, 159

Giavalisco, M. 2002, *ARA&A*, 40, 579

Gilfanov, M., Grimm, H.-J., & Sunyaev, R. 2004, *Nuclear Physics B Proceedings Supplements*, 132, 369

Goldader, J. D., Meurer, G., Heckman, T. M., Seibert, M., Sanders, D. B., Calzetti, D., & Steidel, C. C. 2002, *ApJ*, 568, 651

Grimes, J. P., Heckman, T., Strickland, D., & Ptak, A. 2005, *ApJ*, 628, 187

Heckman, T. M., Armus, L., & Miley, G. K. 1990, *ApJS*, 74, 833

Heckman, T. M., Robert, C., Leitherer, C., Garnett, D. R., & van der Rydt, F. 1998, *ApJ*, 503, 646

Heckman, T. M., Lehnert, M., Strickland, D., & Armus, L. 2000, *ApJS*, 129, 493

Heckman, T. M., Sembach, K. R., Meurer, G. R., Strickland, D. K., Martin, C. L., Calzetti, D., & Leitherer, C. 2001, *ApJ*, 554, 1021

Heckman, T. M., Sembach, K. R., Meurer, G. R., Leitherer, C., Calzetti, D., & Martin, C. L. 2001, *ApJ*, 558, 56

Heckman, T. M., Norman, C. A., Strickland, D. K., & Sembach, K. R. 2002, *ApJ*, 577, 691

Heckman, T. M. 2003, *Revista Mexicana de Astronomia y Astrofisica Conference Series*, 17, 47

Heckman, T. M., et al. 2005, *ApJ*, 619, L35

Helsdon, S. F., & Ponman, T. J. 2000, *MNRAS*, 315, 356

Hoopes, C. G., Heckman, T. M., Strickland, D. K., & Howk, J. C. 2003, *ApJ*, 596, L175

Hoopes, C. G., et al. 2006, in prep

Hurwitz, M., Jelinsky, P., & Dixon, W. V. D. 1997, *ApJ*, 481, L31

Iono, D., Ho, P. T. P., Yun, M. S., Matushita, S., Peck, A. B., & Sakamoto, K. 2004, *ApJ*, 616, L63

Jarrett, T. H., Chester, T., Cutri, R., Schneider, S. E., & Huchra, J. P. 2003, *AJ*, 125, 525

Kennicutt, R. C. 1998, *ApJ*, 498, 541

Kim, D.-C., Sanders, D. B., Veilleux, S., Mazzarella, J. M., & Soifer, B. T. 1995, *ApJS*, 98, 129

Klypin, A., Kravtsov, A. V., Valenzuela, O., & Prada, F. 1999, *ApJ*, 522, 82

Kriss, G. 1994, *ASP Conf. Ser.* 61: *Astronomical Data Analysis Software and Systems III*, 61, 437

Lehmer, B. D., et al. 2005, *AJ*, 129, 1

Lehnert, M. D. & Heckman, T. M. 1996, *ApJ*, 462, 651

Levenson, N. A., Heckman, T. M., Krolik, J. H., Weaver, K. A., & Zycki, P., T. 2006, submitted

Leitherer, C., Ferguson, H. C., Heckman, T. M., & Lowenthal, J. D. 1995, *ApJ*, 454, L19

Loeb, A., & Barkana, R. 2001, *ARA&A*, 39, 19

Malkan, M., Webb, W., & Konopacky, Q. 2003, *ApJ*, 598, 878

Marcolini, A., Strickland, D. K., D'Ercole, A., Heckman, T. M., & Hoopes, C. G. 2005, *MNRAS*, 362, 626

Martin, C. L. 2005, *ApJ*, 621, 227

Martin, D. C., et al. 2005, *ApJ*, 619, L1

Moos, H. W., et al. 2000, *ApJ*, 538, L1

Nandra, K., Mushotzky, R. F., Arnaud, K., Steidel, C. C., Adelberger, K. L., Gardner, J. P., Teplitz, H. I., & Windhorst, R. A. 2002, *ApJ*, 576, 625

Oskinova, L. M., Feldmeier, A., Hamann, W. R. (astro-ph 0603286)

Panagia, N., Fall, S. M., Mobasher, B., Dickinson, M., Ferguson, H. C., Giavalisco, M., Stern, D., & Wiklind, T. 2005, *ApJ*, 633, L1

Peacock, J. A., et al. 2000, *MNRAS*, 318, 535

Pettini, M., Rix, S. A., Steidel, C. C., Adelberger, K. L., Hunt, M. P., & Shapley, A. E. 2002, *ApJ*, 569, 742

Robertson, B., Bullock, J. S., Font, A. S., Johnston, K. V., & Hernquist, L. 2005, *ApJ*, 632, 872

Rupke, D. S., Veilleux, S., & Sanders, D. B. 2005, *ApJS*, 160, 115

Sanders, D. B. & Mirabel, I. F. 1996, *ARA&A*, 34, 749

Sako, M., Kahn, S. M., Paerels, F., Liedahl, D. A., Watanabe, S., Nagase, F., & Takahashi, T. 2002, High Resolution X-ray Spectroscopy with XMM-Newton and Chandra

Scannapieco, C., Tissera, P. B., White, S. D. M., & Springel, V. 2005, *MNRAS*, 907

Schild, H., et al. 2004, *A&A*, 422, 177

Shapley, A. E., Steidel, C. C., Pettini, M., & Adelberger, K. L. 2003, *ApJ*, 588, 65

Soifer, B. T., Boehmer, L., Neugebauer, G., & Sanders, D. B. 1989, *AJ*, 98, 766

Sommer-Larsen, J., Gelato, S., & Vedel, H. 1999, *ApJ*, 519, 501

Springel, V., et al. 2005, *Nature*, 435, 629

Steidel, C. C., Adelberger, K. L., Giavalisco, M., Dickinson, M., & Pettini, M. 1999, *ApJ*, 519, 1

Steidel, C. C., Pettini, M., & Adelberger, K. L. 2001, *ApJ*, 546, 665

Stiavelli, M., Fall, S. M., & Panagia, N. 2004, *ApJ*, 610, L1

Strickland, D. K., & Stevens, I. R. 2000, *MNRAS*, 314, 511

Sutherland, R. S., & Dopita, M. A. 1993, *ApJS*, 88, 253

Tamura, T., Kaastra, J. S., den Herder, J. W. A., Bleeker, J. A. M., & Peterson, J. R. 2004, *A&A*, 420, 135

Tremonti, C. A., et al. 2004, *ApJ*, 613, 898

Veilleux, S., Cecil, G., & Bland-Hawthorn, J. 2005, *ARA&A*, 43, 769

York, D. G., et al. 2000, AJ, 120, 1579

Yun, M. S., Scoville, N. Z., & Knop, R. A.
1994, ApJ, 430, L109

TABLE 1
BASIC PROPERTIES OF VV 114

	Position J2000		cz ^a km/s	Scale kpc/''	Z ^b	L _{FIR} ^c L _⊙	L _K ^c L _⊙	L _{FUV} ^d L _⊙	r _{50,UV} ^d kpc	I _{FUV} ^c L _⊙ /kpc ²
Global	+1 07 47.1	-17 30 24.3	6040	0.41	8.6-8.7	2.8×10^{11}	2.1×10^{10}	3.2×10^{10}		
East	+1 07 47.6	-17 30 25.8						1.0×10^{10}	4	9.9×10^7
West	+1 07 46.6	-17 30 24.0						2.2×10^{10}	2.3	5.6×10^8

^aYun et al. (1994).

^bGas phase metallicity as log(O/H)+12 from Kim et al. (1995) using the transformations of Charlot & Longhetti (2001).

^cIRAS (Soifer, Boehmer, Neugebauer, & Sanders 1989) and 2Mass (Jarrett et al. 2003) results are transformed using methods of Sanders & Mirabel (1996) and Carpenter (2001) respectively.

^dResults derived from Goldader et al. (2002).

TABLE 2
SINGLE COMPONENT ISM ABSORPTION LINE FIT DATA

Ion	λ_0 Å	$\log(\lambda f N/N_H)$	Instrument	W_λ Å	v_c km/s	FWHM km/s
Ly β	1025.722	1.909	lif1a	3.8 ± 0.5	5975 ± 24	728 ^a
			lif2b	3.9 ± 0.6	5962 ± 34	728 ^a
C III	977.02	-0.608	lif1a	3.2 ± 0.8	5915^b	700 ^b
			lif2b	3.6 ± 1.4	5929 ± 59	700 ^b
O VI	1031.926	-1.133	lif1a	1.8 ± 0.1	5771^a	700 ^b
			lif2b	2.0 ± 0.1	5845^a	700 ^b
C II	1036.337	-1.374	lif1a	2.8 ± 0.2	6011 ± 17	655 ± 59
			lif2b	2.8 ± 0.2	5978 ± 24	658 ± 80
O I	988.733	-1.564	lif1a	1.6 ± 0.4	5935 ± 30	700 ^b
			lif2b	2.2 ± 0.4	5932^a	700 ^b
N II	1083.99	-2.002	lif1b	2.5 ± 0.1	5954 ± 22	693 ^a
			lif2a	2.6 ± 0.1	5949 ± 19	683 ^a
N III	989.799	-2.027	lif1a	2.8 ± 0.2	5935^a	700 ^b
			lif2b	1.8 ± 0.4	5932^c	700 ^b
N I	1134.415	-2.089	lif1b	1.0 ± 0.2	5917 ± 47	700 ^b
			lif2a	1.1 ± 0.2	5918 ± 34	656 ± 116
O I	1039.23	-2.290	lif1a	0.8 ± 0.2	6011^d	655^d
			lif2b	0.8 ± 0.2	5978^d	658^d
Fe II ^d	1144.938	-2.420	lif1b	1.3 ± 0.1	5698^a	700 ^b
			lif2a	1.1 ± 0.1	5790^a	700 ^b

^aUnable to determine errors on this value.

^bUnable to accurately determine value so FWHM fixed to 700 km/s

^dO I λ 1039 values tied to velocity shift and FWHM of the C II λ 1036 line.

^cN III λ 990 values tied to velocity shift of the O I λ 989 line.

^dFe II λ 1144 line measurements are strongly affected by the second order airglow emission line He I λ 584 and an instrumental artifact that causes a break in the continuum

TABLE 3
TWO COMPONENT ABSORPTION LINE FITS

Ion	λ_0 Å	$\log(\lambda f N/N_H)$	Instrument	Galaxy			Outflow		
				W_λ Å	v_c km/s	FWHM km/s	W_λ Å	v_c km/s	FWHM km/s
C II	1036.337	-1.374	lif1a	2.2 ± 0.4	6081 ± 32	429 ± 85	0.9 ± 0.5	5663 ± 126	420 ± 140
			lif2b	2.2 ± 0.6	6079 ± 17	411 ± 143	1.3 ± 0.5	5697 ± 97	503 ± 176
N II	1083.99	-2.002	lif1b	1.8 ± 0.1	6019 ± 11	499 ± 49	0.7 ± 0.3	5623 ± 117	349 ^a
			lif2a	2.0 ± 0.1	6008 ± 31	529 ± 57	0.8 ± 0.4	5681 ± 178	408 ^a
N I	1134.415	-2.089	lif1b	0.6 ± 0.2	6076 ± 45	318 ± 90	0.4 ± 0.2	5669 ± 73	302 ± 145
			lif2a	0.7 ± 0.2	6035 ± 49	372 ± 101	0.3 ± 0.2	5669 ± 60	270 ± 165
O I	1039.23	-2.290	lif1a	0.7 ± 0.2	6081 ^b	429 ^b	0.3 ± 0.2 ^b	5663 ^b	420 ^b
			lif2b	0.7 ± 0.3	6079 ^b	411 ^b	0.2 ± 0.4	5697 ^b	503 ^b

^aUnable to determine errors on this value.

^bO I λ 1039 values tied to equivalent value of the C II λ 1036 line.

TABLE 4
STELLAR PHOTOSPHERIC ABSORPTION LINE FIT DATA

Ion	λ_0 Å	Instrument	W_λ Å	v_c km/s	FWHM km/s
Si IV	1122.487	lif1b	1.1 ± 0.1	5967 ± 22	390 ^a
		lif2a	1.0 ± 0.1	5974 ± 18	374 ± 42
Si IV	1128.201	lif1b	0.8 ± 0.1	5967 ^b	390 ^b
		lif2a	0.7 ± 0.1	5974 ^b	389 ^a
P V	1117.977	lif1b	0.3 ± 0.1	5960 ^a	390 ^c
		lif2a	0.3 ± 0.1	5950 ^a	390 ^c

^aUnable to determine errors on this value.

^bValue tied to velocity shift or FWHM of the Si IV $\lambda 1122$ line.

^cUnable to accurately determine value so FWHM fixed to 390 km/s

TABLE 5
X-RAY SPECTRAL FITS

Region	Instr.	Position ^a J2000		Radius ^a "	N_H 10^{22} cm^{-2}	kT keV	K^b	α/Fe	N_H 10^{22} cm^{-2}	PL Norm ^c	Γ	χ^2/DOF
VV 114 ^d	Chandra	01:07:47.0	-17 30 29.0	24.3	5.7×10^{-2}	$0.62^{+0.03}_{-0.03}$	$2.6^{+0.7}_{-1.0} \times 10^{-4}$	$2.7^{+0.6}_{-0.7}$	$0.6^{+0.3}_{-0.3}$	$9.2^{+4}_{-3} \times 10^{-5}$	$2.0^{+0.3}_{-0.2}$	121/128
VV 114 ^d	XMM	01:07:47.0	-17 30 29.0	24.3	5.7×10^{-2}	$0.59^{+0.06}_{-0.07}$	$2.5^{+2.5}_{-2.5} \times 10^{-4}$	$2.2^{+2.00}_{-0.73}$	$1.1^{+1.1}_{-0.7}$	$2.2^{+4.5}_{-1.1} \times 10^{-4}$	$2.8^{+1.2}_{-1.5}$	100/117
VV 114E ^e	Chandra	01 07 47.5	-17 30 25.6	4.4	5.7×10^{-2}	$0.30^{+0.75}_{-0.2}$	$1.7^{+6.0}_{-1.4} \times 10^{-4}$	5.0 ^f	$1.5^{+3.4}_{-1.0}$	$1.7^{+2.2}_{-1.1} \times 10^{-5}$	$1.3^{+0.2}_{-0.5}$	13/16

^aCenter and Radius of circular region used to extract fitted spectra.

^bPlasma model normalization in units of $\frac{10^{-14}}{4\pi[D_A(1+z)]^2} \int n_e n_H dV$, where D_A is the angular distance, and n_H and n_e are the hydrogen and electron number densities respectively.

^cphotons $\text{keV}^{-1} \text{ cm}^{-2} \text{ s}^{-1}$ at 1 keV

^dValues derived from an xspec model of wabs1 (vmekal + zwabs2 (powerlaw)) using default abundances angr (Anders & Grevesse 1989).

^eValues derived from an xspec model of wabs1 (zwabs2 (vmekal + gaussian1 + gaussian2) + zwabs3 (powerlaw)) using default abundances angr (Anders & Grevesse 1989). The gaussians were centered at 1.83 keV and 1.39 keV with equivalent widths of 1.67 keV and .31 keV respectively. The derived value for the other intrinsic column absorber for the thermal component and line emission was $N_H \sim 8 \times 10^{21} \text{ cm}^{-2}$.

^fAs we observe photoionized emission in VV 114E it is not clear that the α/Fe ratio of the vmekal model is physically meaningful.

TABLE 6
MASS AND ENERGY OUTFLOW RATES

Ion	$N_{\text{Ion}}^{\text{a}}$ 10^{14} cm^{-2}	Abundance ^b $\log(N_{\text{Elem}}/N_{\text{H}}) + 12$	N_{H} 10^{18} cm^{-2}	$\frac{\Omega}{4\pi} \dot{M}^{\text{c}}$ $\text{M}_{\odot}/\text{yr}$	$\frac{\Omega}{4\pi} \dot{E}^{\text{c}}$ 10^{40} ergs/s
O VI	21	8.66	>23	>2.6	>13
N II	8.4	7.78	14	1.54	7.8
N I	4.3	7.78	7.1	0.79	4.0
N I+N II	13	7.78	21	2.3	12
C II	13	8.39	5.1	0.56	2.9
Total Cool Gas ^d			>44	>4.9	>25
Total Hot Gas ^e				$50f^{1/2}$	$500f^{1/2}$

^aBased on outflow equivalent width and FWHM from Table 3.

^bAsplund et al. (2005)

^cEstimated mass and kinetic energy outflow rates (see text).

^dFrom FUSE data

^eFrom X-ray data. Note that f is the volume filling factor of the hot gas.

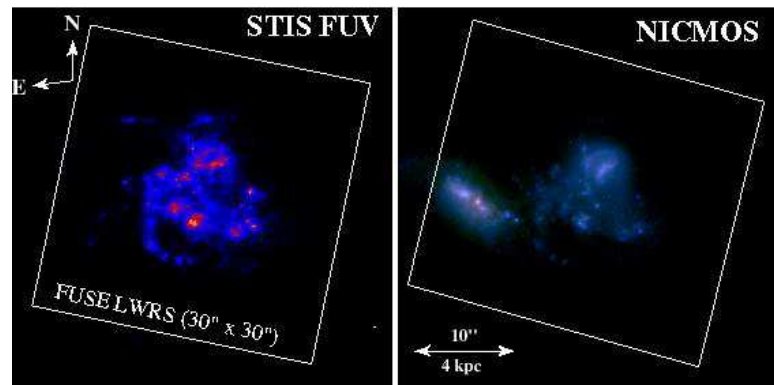


Fig. 1.— FUSE LWRS aperture overlaid on a HST STIS FUV and NICMOS falsecolor image. Only the western component is visible in the FUV image. Both images are from Goldader et al. (2002) and use a logarithmic scale map. The NICMOS falsecolor image is an overlay of the F110W ($1.025\mu\text{m}$), F160W ($1.55\mu\text{m}$), and F222M ($2.3\mu\text{m}$) images as the blue, green, and red respectively.

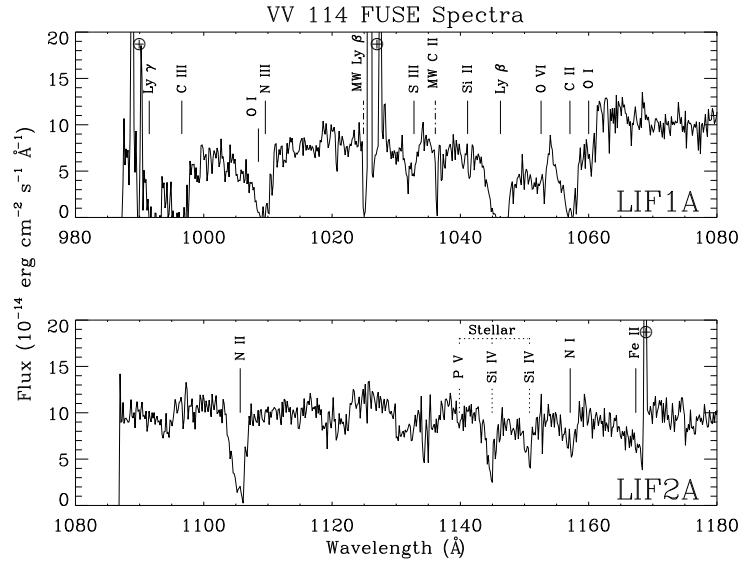


Fig. 2.— Smoothed spectra of VV 114 from the LiF1A and LiF2A channel segments of VV 114. Prominent ISM, stellar photospheric, milky way, and airglow lines have been marked.

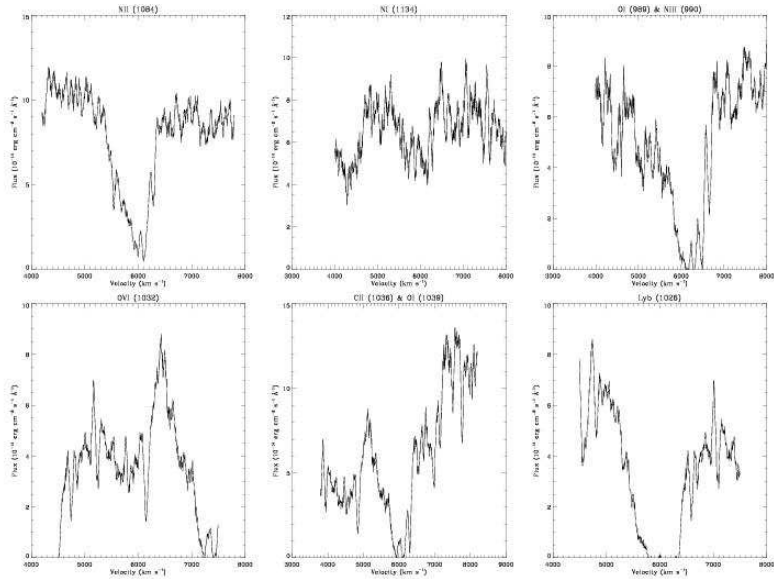


Fig. 3.— Absorption line profile of some of the most prominent lines. Two blended absorption lines have been plotted, C II λ 1036 and O I λ 1039, and O I λ 989 and N III λ 990. The spectra have been smoothed by a factor of 8.

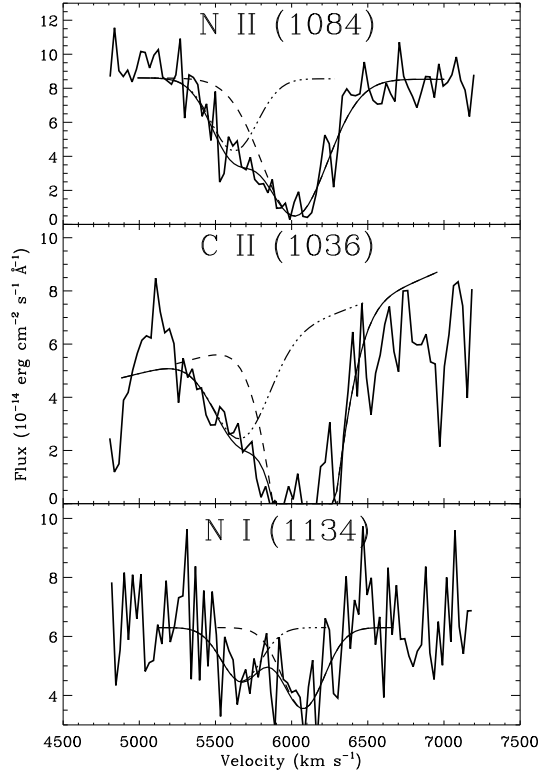


Fig. 4.— These three absorption lines show several similar absorption line features. All three lines have a blueshifted component in addition to a stronger component associated with the galaxy. The dashed lines represent the two absorption lines fit to the data while the solid line is the total fit. Note that the C II $\lambda 1036$ is mildly blended with the O I $\lambda 1039$. For comparison, the galaxy systemic velocity based on mm-wave CO observations is $v_{sys} \simeq 6050$ km/s while stellar photospheric lines in the FUSE spectrum yield $v_{sys} \simeq 5970$ km/s. The spectra have been binned by a factor of 10.

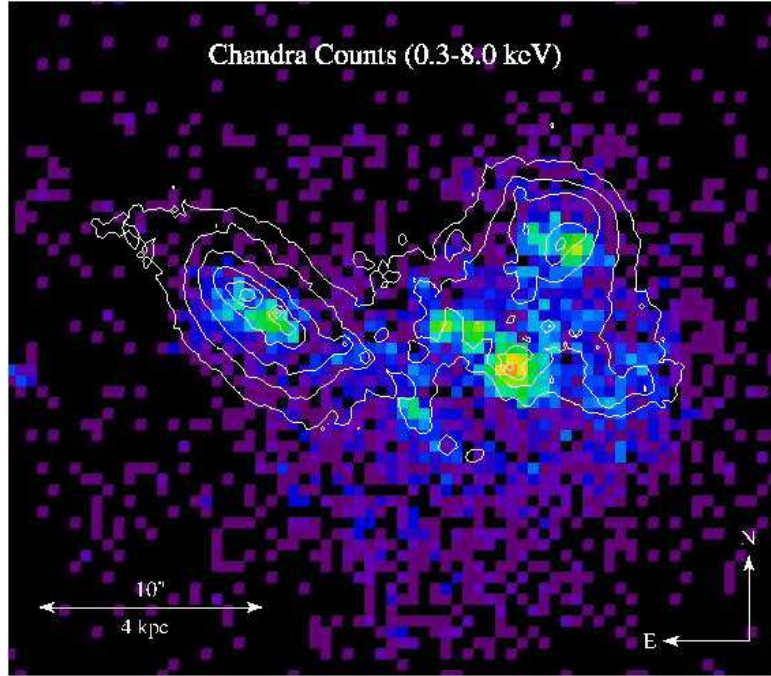


Fig. 5.— Here we have displayed the *Chandra* 0.3-8.0 keV X-ray counts image. The NICMOS F160W (1.55 μ m) image of VV 114 is overlayed for comparison. Both are displayed using a logarithmic scale. The western component of VV 114 dominates the X-ray emission. The X-ray emission of the western component has a similar morphology to the FUV STIS image in Figure 1. Diffuse X-ray emission can also be seen extending south of the galaxy. The eastern component of the galaxy is also clearly seen in the X-ray image.

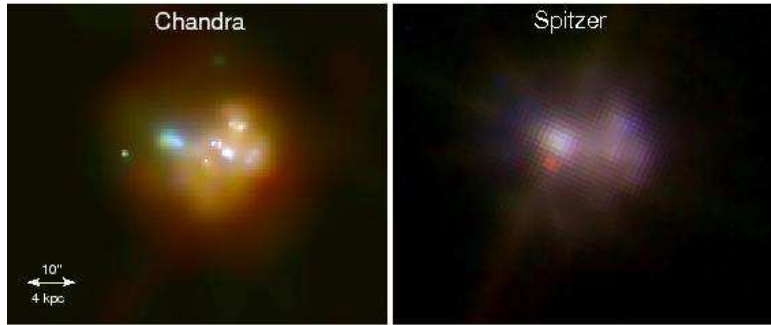


Fig. 6.— *Chandra* and Spitzer IRAC false color images of VV 114. The *Chandra* image has been adaptively smoothed and constructed using 0.3-1.0, 1.0-2.0, and 2.0-8.0 keV as the red, green, and blue colors respectively. Red, green, and blue are mapped to channels 4 (8 μ m), 3 (5.8 μ m), and 1 (3.6 μ m) in the Spitzer IRAC image. The Chandra image shows strong absorption of the emission from the eastern component. A point source is coincident with the unresolved source also seen at the center of VV 114E in the NICMOS and Spitzer images.

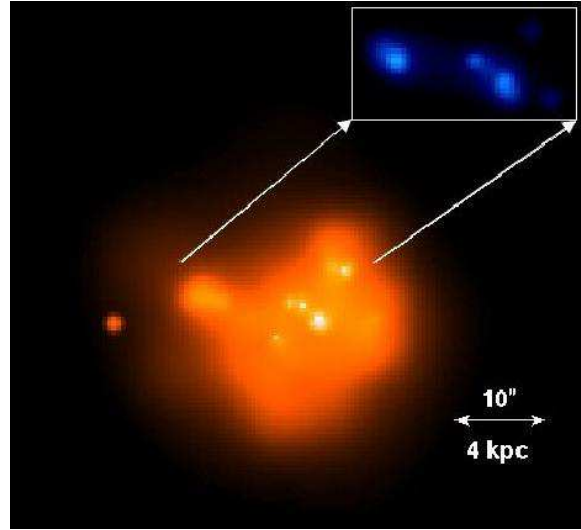


Fig. 7.— A smoothed soft band (0.3-2.0 keV) *Chandra* image of VV 114 shows that soft emission extends far beyond the central regions. A blown up image of the 3-8 keV central region is displayed in the upper right corner. This small region contains all of the observed hard X-ray emission in VV 114. In the hard X-ray image VV 114E has a higher peak brightness and is significantly more compact than VV 114W. They have comparable hard X-ray fluxes while the heavily absorbed VV 114E is barely observed in the soft band. Both images are plotted on a log scale.

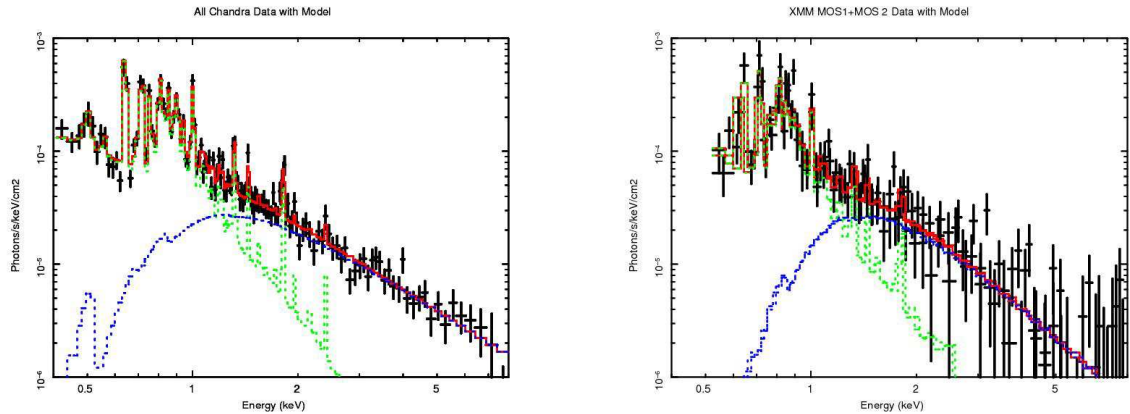


Fig. 8.— The total *Chandra* and *XMM-Newton* MOS+MOS2 unfolded spectra of VV 114 with total fit (red), thermal vmekal component (green), and powerlaw component (blue). The spectra are comparable and are both well modelled by a thermal plasma ($kT \sim 0.6$ keV) plus a powerlaw with intrinsic absorption.

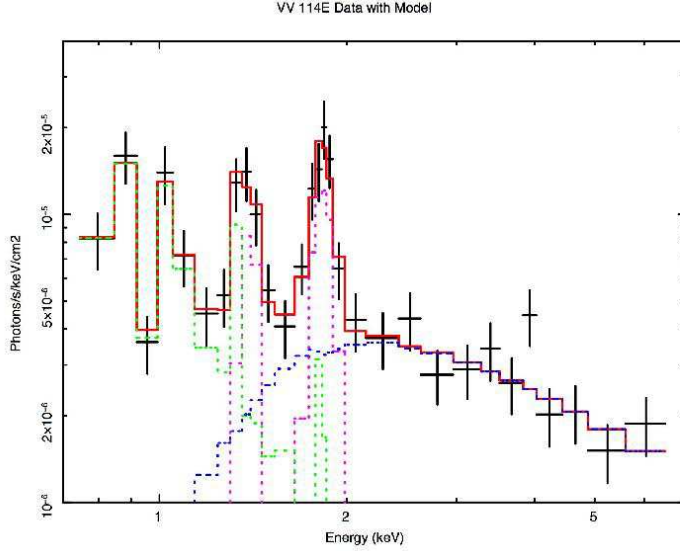


Fig. 9.— The *Chandra* unfolded spectra of VV 114E with total fit (red), thermal vmekal component (green), powerlaw component (blue), and two gaussians (purple). The powerlaw is fairly flat with a photon index of 1.3 and intrinsic absorber with $N_H \sim 2 \times 10^{22} \text{ cm}^{-2}$. The two gaussians fit the enhanced Si ($\sim 1.4 \text{ keV}$) and Mg ($\sim 1.8 \text{ keV}$) which are typical in photo-ionized regions.

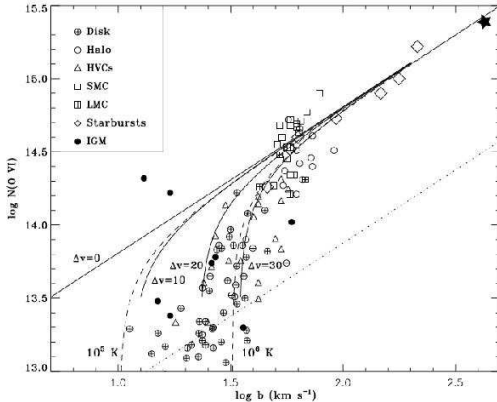


Fig. 10.— Column density vs. line width for a wide variety of O VI absorption line systems including galactic disk and halo, high velocity clouds, starburst galaxies, and the IGM. The two dashed lines indicate the predictions for radiatively cooling gas for assumed temperatures of $T_{OVI} = 10^5$ & 10^6 K. This plot is originally from (Heckman et al. 2002). VV 114 has been added and is represented by the star in the upper right. VV 114 extends the relationship between flow velocity and column density to significantly higher values.

Thermal X-ray and FIR Luminosities Divided by K-Band Luminosity

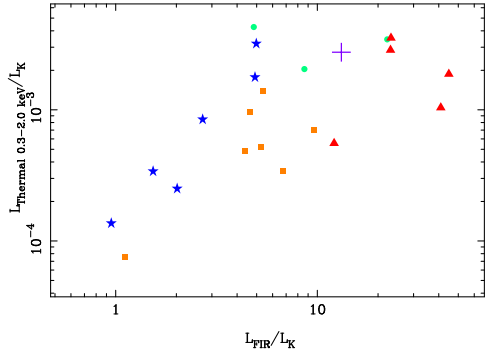


Fig. 11.— In this plot taken from Grimes et al. (2005) we have divided both the thermal X-ray (0.3-2.0 keV) and the FIR luminosity by the K-Band luminosity (a proxy for stellar mass). The FIR luminosity of the dwarf starbursts is actually the sum of the their UV and FIR luminosities. There is a clear linear relation between the SFR per stellar mass and the thermal X-ray emission per stellar mass. The IRAS and K-Band data was obtained from *NED* and have been transformed using the methods of Sanders & Mirabel (1996) and Carpenter (2001) respectively. VV 114 follows the scaling relation defined by starbursts. Key: Orange Squares-Dwarf Starbursts, Blue Stars-Starbursts, Red Triangles-ULIRGs, Green Circles-AGN ULIRGs, Purple Cross-VV 114

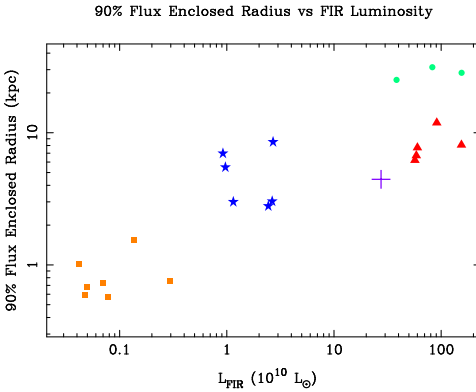


Fig. 12.— 90% Flux Enclosed Radii in the 0.3-1.0 keV band vs FIR luminosities (see Grimes et al. (2005) for details). The size of the X-ray emitting region is correlated with the SFR rate as measured by the FIR luminosity. VV 114 falls on the lower edge of the relation possibly as the soft X-ray band is only detectable in VV 114W while the FIR luminosity traces the SFR of the entire galaxy. The displayed FIR luminosities of the dwarf starbursts are actually the sum of their UV and FIR luminosities. We use their bolometric luminosity to account for the lower dust content in dwarfs. Key: Orange Squares-Dwarf Starbursts, Blue Stars-Starbursts, Red Triangles-ULIRGs, Green Circles-AGN ULIRGs, Purple Cross-VV 114

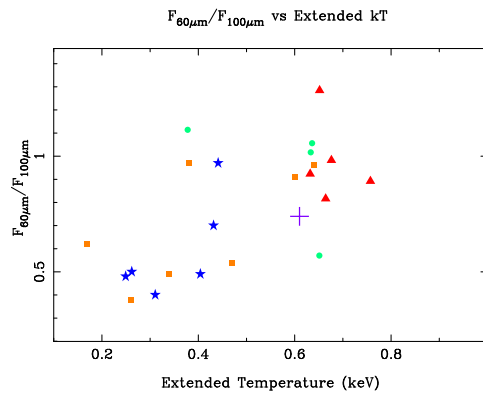


Fig. 13.— $F_{60\mu\text{m}}/F_{100\mu\text{m}}$ vs X-ray Gas Temperature. The $F_{60\mu\text{m}}/F_{100\mu\text{m}}$ ratio is an indicator of dust temperature and hence the star formation rate per unit area. There is a correlation between gas and dust temperature. VV 114 follows the same correlation as the starbursts. Key: Orange Squares-Dwarf Starbursts, Blue Stars-Starbursts, Red Triangles-ULIRGs, Green Circles-AGN ULIRGs, Purple Cross-VV 114